FRONTIERS OF PHYSICS

RESEARCH ARTICLE
Volume 21 / Issue 5 / 055203 / 2026

Modulating spin relaxation at the ferromagnet/molecule interface via anchoring atom engineering

Xurong Shi[1,4], Shen Wang[2,3,†], Kai Li[5], Chengdong Mi[1,4], Jinrong Wang[1,4]

1 Department of Physics and Electronic Information Engineering, Lyuliang University, Lishi 033001, China
2 School of Physics and Electronics Engineering, Shanxi University, Taiyuan 030006, China
3 State Key Laboratory of Quantum Optics and Quantum Optics Devices, Shanxi University, Taiyuan 030006, China
4 Lvliang City Key Laboratory of Quantum Precision Measurement, Lyuliang University, Lishi 033001, China
5 College of Physics, Changchun Normal University, Changchun 130032, China
Corresponding author. E-mail: †shenwang@sxu.edu.cn
Received October 24, 2025; accepted March 17, 2026

ABSTRACT

Although spintronics has demonstrated potential for high-density, low-power electronic devices, performance often falls short of theoretical predictions owing to challenges in efficient spin injection and transport. Prior research has highlighted the role of molecular design in modulating interfacial properties; nonetheless, the impact of different anchoring atoms on spin relaxation, particularly during tunneling transport, remains largely unexplored. We fabricated Fe_3O_4/molecule hybrid nanoparticles through self-assembly to investigate experimentally and theoretically how different anchoring atoms — S and C (–COOH, $–SO_3H$, $–OSO_3H$) — affect the electrical and magneto-transport properties at the Fe_3O_4/molecule interface, as well as intramolecular spin relaxation and the associated physical mechanisms. Electrical transport measurements revealed that the contact resistivity at the Fe_3O_4/molecule interface was highly sensitive to the anchoring groups, in marked contrast to the tunnel attenuation coefficient β. Meanwhile, magneto-transport results demonstrated that replacing the carbon-centered anchoring group (–COOH) with sulfur-centered groups ($–SO_3H$, $–OSO_3H$) reduced the magnetoresistance and shortened the intramolecular spin diffusion length by ~69% compared with the carbon-centered anchoring group (–COOH). The theoretical studies clarified the role of orbital hybridization in tuning interfacial spin properties. We also examined the influence of magnetic field and temperature on intramolecular spin relaxation during tunneling and discussed the underlying mechanisms. This study experimentally verified, for the first time, the occurrence of spin relaxation within organic molecules during tunneling.

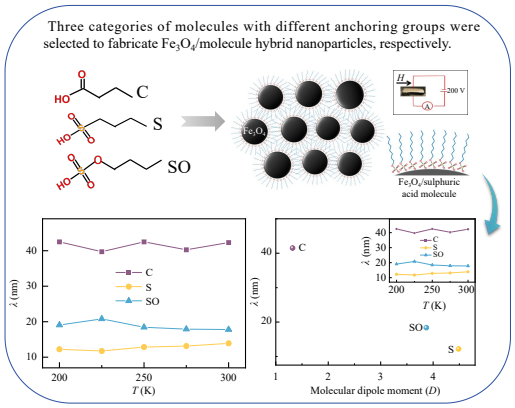

Keywords organic spintronics, spin-dependent tunneling, spin relaxation, Fe_3O_4/molecule interface, anchoring atom

1 Introduction

Spintronics, a prominent branch of microelectronics, focuses on utilizing electron spins for information storage, transmission, and processing [1, 2]. Compared with conventional electronics, spintronic devices offer significant

https://doi.org/10.15302/frontphys.2026.055203

advantages, including higher storage density and lower energy consumption, and have become one of the most active research frontiers [3–5]. Expanding beyond conventional rigid systems, several studies has shifted towards flexible spintronics for wearable applications [6, 7]. For instance, Fe_3O_4 films prepared at room temperature on polymer substrates not only retain half-metallic properties and high magnetoresistance, but also exhibit excellent mechanical flexibility [8–10]. In spintronics, the representative device structure is the spin valve, composed of two ferromagnetic electrodes sandwiching a non-magnetic layer, which enables spin–charge interaction by combining magnetic response with charge-related properties [11]. A key prerequisite for realizing these functions is the effective injection of spin-polarized charge carriers into non-magnetic spacers [12], followed by their sustained transport while maintaining spin coherence [13]. However, despite extensive research efforts, the performance of spintronic devices remains below theoretical expectations because of persistent challenges in charge and spin injection efficiency [14].

Theoretical studies [15, 16] have demonstrated that unique spin-related functions can be achieved at ferromagnet/molecule interfaces — capabilities unattainable at conventional ferromagnetic/inorganic interfaces — making these interfaces critical platforms for spin injection and manipulation at the molecular scale. The ferromagnet/molecule interface can be engineered to effectively modulate magnetic properties, a prerequisite for enhancing spin injection efficiency and optimizing device performance [17, 18]. Given the chemical diversity of organic molecules, substantial potential exists to regulate spin injection and interfacial properties through molecular design. This capability opens new avenues for information storage and transmission, thereby driving growing research interest in this field [19, 20]. Among several molecular components, the anchoring group serves as a vital bridge between the molecule and ferromagnetic electrode, directly determining the bonding mode, bonding strength, and orbital hybridization at the interface [21], and thus fundamentally influencing interfacial spin injection efficiency and spin transport characteristics in molecular junctions [22]. Zhang *et al.* [23] employed *ab initio* theory to investigate the spin characteristics of organic molecules adsorbed on the Ni(111) surface and demonstrated that interfacial spin polarization is highly sensitive to the hybridization of the anchoring atom's outer orbitals and their energy level alignment relative to the *d*-orbitals of ferromagnetic atoms. Their study further revealed that spin polarization depends on the atomic species, and that anchoring atoms with high electronegativity can yield enhanced tunneling magnetoresistance and large spin-filtering efficiency. In addition, numerous theoretical works [24, 25] have demonstrated that modifying the anchoring group is among the most direct and effective strategies for tuning spin injection at ferromagnet/molecule interfaces. Collectively, these findings provide crucial insights and guidance for advancing spintronics and optimizing the performance of spin-based devices.

Spin relaxation in organic molecules constitutes a critical aspect of spin transport processes. To the best of our knowledge, current research on the mechanisms of spin relaxation predominantly focuses on carrier hopping or diffusion transport within molecules [26, 27], whereas only a few studies have examined tunneling transport in molecules. As one of the principal transport modes in organic spin devices, tunneling is commonly observed at ferromagnet/molecule interfaces and in single-molecule junctions. Consequently, investigating spin relaxation mechanisms in tunneling processes is essential for optimizing spin injection and transport efficiency and for deepening the understanding of organic spintronics. In this work, we fabricated Fe_3O_4/carboxylic acid, Fe_3O_4/sulfonic acid, and Fe_3O_4/sulfuric acid hybrid nanoparticle samples via self-assembly to systematically investigate the effects of different anchoring atoms (C and S) on spin transport at the Fe_3O_4/molecule interface and the mechanisms of intramolecular spin relaxation during tunneling. Electrical transport measurements revealed that the potential barrier at the Fe_3O_4/molecule interface was highly sensitive to the anchoring groups. Furthermore, magneto-transport results demonstrated that replacing replacing the carbon-centered anchoring group (–COOH) with sulfur-centered groups (–SO_3H, –OSO_3H) reduced the magnetoresistance and shortened the intramolecular spin diffusion length by ~69%. The density functional theory (DFT) be incorporated to clarify the role of orbital hybridization in tuning interfacial spin properties. Furthermore, we analyzed the roles of magnetic field and temperature in intramolecular spin relaxation during tunneling and discussed the underlying mechanisms.

2 Experimental methods

The detailed fabrication process of Fe_3O_4/molecule hybrid nanoparticles has been described previously [28], where the average size of the Fe_3O_4 particles was ~10 nm [29]. We selected three categories of molecules with different anchoring groups (–COOH, –SO_3H, –OSO_3H), namely *N*-alkyl carboxylic acids, *N*-alkyl sulfonic acids, and *N*-alkyl sulfuric acids, as shown in Figs. 1(a), (b), and (c), respectively. The *N*-alkyl carboxylic acids include butanoic acid ($CH_3(CH_2)_2COOH$), octanoic acid ($CH_3(CH_2)_6COOH$), dodecanoic acid ($CH_3(CH_2)_{10}COOH$), and octadecanoic acid ($CH_3(CH_2)_{16}COOH$), denoted as C*n*, where $n = 4$, 8, 12, and 18, respectively. The *N*-alkyl sulfonic acids include butane sulfonic acid ($CH_3(CH_2)_3SO_3H$), octane sulfonic acid ($CH_3(CH_2)_7SO_3H$), dodecyl sulfonic acid

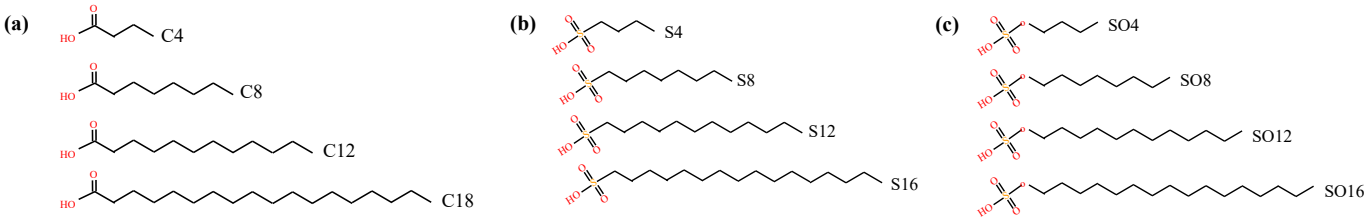

Fig. 1 Four different lengths of carboxylic acids **(a)**, sulfonic acids **(b)**, and sulfuric acids **(c)** were chosen as the coated molecules.

$(CH_3(CH_2)_{11}SO_3H)$, and hexadecyl sulfonic acid $(CH_3(CH_2)_{15}SO_3H)$, denoted as Sn, where n = 4, 8, 12, and 16, respectively. The *N*-alkyl sulfuric acids include butane sulfate acid $(CH_3(CH_2)_3OSO_3H)$, octane sulfate acid $(CH_3(CH_2)_7OSO_3H)$, dodecyl sulfate acid $(CH_3(CH_2)_{11}OSO_3H)$, and hexadecyl sulfate acid $(CH_3(CH_2)_{15}OSO_3H)$, denoted as SOn, where n = 4, 8, 12, and 16, respectively. Fe_3O_4 nanoparticles coated with Cn, Sn, and SOn were denoted as S(Cn), S(Sn), and S(SOn), respectively. The samples formed a magnetic tunnel junction network in which Fe_3O_4 nanoparticles were coated with monolayer molecules [29, 28], as shown in Fig. 2(a). Electrons preferentially take tunneling paths with the minimum particle-to-particle separation — corresponding to the molecular length — so [30], the transport measurements reflect molecular-scale characteristics. All samples were fabricated in ambient air and measured in a vacuum.

3 Results and discussion

3.1 Electrical transport

First, we investigated the electrical transport properties of these samples, as shown in Fig. 2(b), which depicts the dependence of resistivity (ρ) on molecular length (d) for S(Cn), S(Sn), and S(SOn). All curves followed $\rho \sim e^{-\beta d}$ (β is the attenuation coefficient), indicating that carriers tunnel through the molecules from one Fe_3O_4 particle to another, as previously demonstrated [28]. The temperature-independent β further supports the tunneling transport characteristics. The measured values were β_C = 0.21 Å^{-1}, β_S = 0.26 Å^{-1}, and β_{SO} = 0.23 Å^{-1}, showing subtle differences among samples with different anchoring groups. In addition, the relationship $\beta_S > \beta_{SO} > \beta_C$ suggests that the dominant carrier transport mechanism within the molecules is unlikely to be intermolecular tunneling [31], further discussion can be found in Part 2 of the Supplementary Materials.

As shown in Fig. 3(a), the ultraviolet photoelectron spectroscopy (UPS) measurements show that the work function of bare Fe_3O_4 is 5.65 eV, whereas those of S(C12), S(S12), and S(SO12) are 7.22, 6.95, and 7.10 eV, respectively, which are 1.57, 1.30, and 1.45 eV higher than that of Fe_3O_4, respectively. This increase in the work functions is attributed to the formation of a dipole moment at the Fe_3O_4/molecule interface; owing to this dipole moment, the fermi level (E_F) of Fe_3O_4 moves further away from the vacuum energy level. The calculated energy levels and lengths of these molecules are shown in Table 1. Compared to the lowest occupied molecular orbitals (LUMO) of these molecules, their highest occupied molecular orbitals (HOMO) are closer

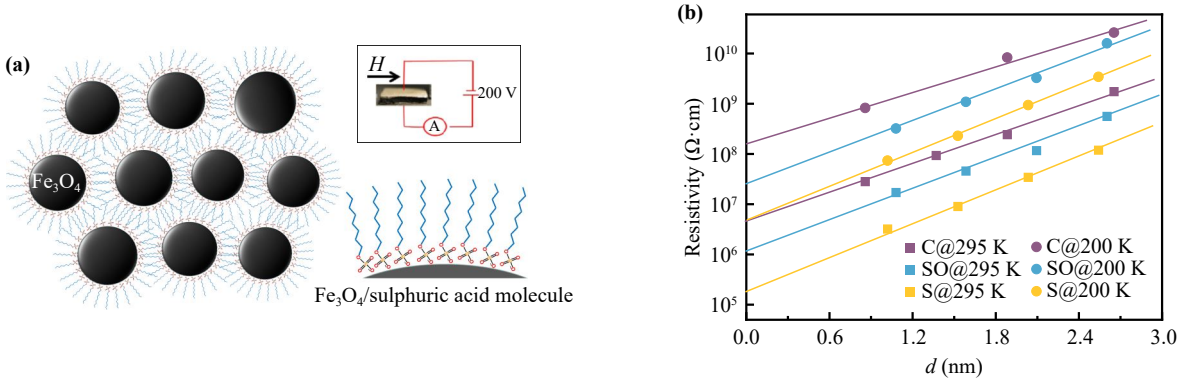

Fig. 2 **(a)** Schematic illustration of Fe_3O_4/sulfuric acid hybrid nanoparticles, similar to the structures of Fe_3O_4/sulfonic acid and Fe_3O_4/carboxylic acid analogues, the inset displays the circuit configuration used for the transport measurements of the sample. **(b)** Dependence of resistivity (ρ) on the molecular length (d) for S(Cn), S(Sn), and S(SOn), where carboxylic acid sample measured at 295 K were represented by C@295 K (purple square).

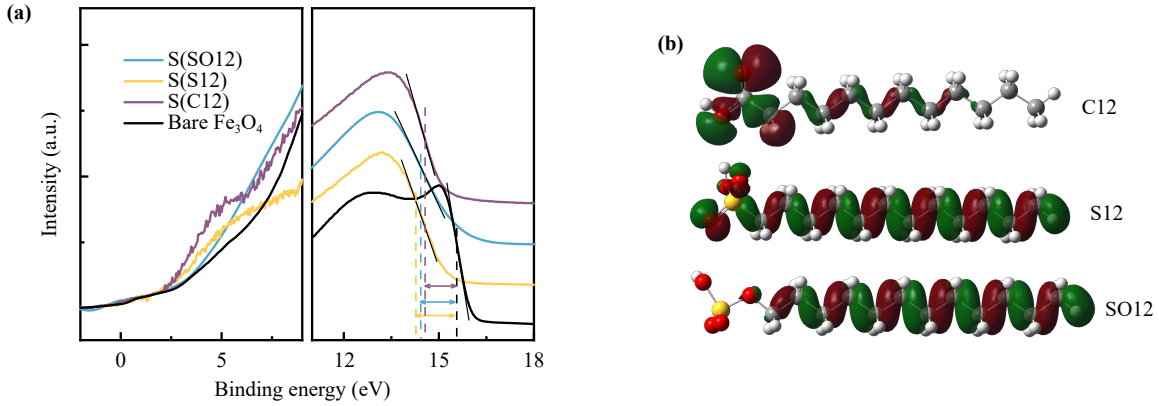

Fig. 3 **(a)** HeI UPS profiles for bare Fe_3O_4, S(S12), S(SO12), and S(C12). **(b)** Spatial distribution of the HOMO of the C12, S12, and SO12 molecules.

Table 1 Calculation results of the isolated carboxylic acids, sulfonic acids and sulfuric acids.

	Molecule	HOMO (eV)	LUMO (eV)	Length (Å)	Gap (eV)	Dipole moment (D)
C	C4	–7.95	–0.29	8.58	7.66	1.35
	C12	–7.91	–0.19	18.83	7.72	1.32
S	S4	–8.68	–0.50	10.19	8.18	4.20
	S12	–8.30	–0.48	20.34	7.82	4.44
SO	SO4	–8.68	–0.68	10.80	8.00	3.73
	SO12	–8.31	–0.67	20.94	7.64	3.91

to E_F of Fe_3O_4, indicating that the HOMO mainly participates in the tunneling transport. Combining the UPS measurements results and the calculated molecular energy levels indicates that the energy level differences ΔE between the Fermi surface and molecular HOMOs are as follows: $\Delta E(C) = 0.69$ eV, $\Delta E(S) = 1.35$ eV, and $\Delta E(SO) = 1.21$ eV. The observed trend $\Delta E(S) > \Delta E(SO) > \Delta E(C)$ could possibly explain the weak correlation between the anchoring groups and β values ($\beta_S > \beta_{SO} > \beta_C$) [32].

The DFT calculations for these complexes were performed using the Guassian16 package [33]. The geometry optimizations and frequency calculations were conducted using the B3LYP/6-311+G(d, p) basis sets [34, 35]. For more calculated molecular energy level, please refer to Part 1 of the Electronic Supplementary Materials.

Interestingly, the contact resistivity ρ_c of three categories of samples is more sensitive to anchoring group, as depicted in Fig. 2(b), ρ_c(–COOH) > ρ_c(–OSO_3H) > ρ_c(–SO_3H). Among these three categories of samples, the Fe_3O_4/sulfonic acid interface exhibits a relatively smaller hindrance effect on carrier transport, which was more conducive to charge injection, followed by the Fe_3O_4/sulfuric acid. However, the order of contact resistivity magnitudes is opposite to that of the contact barrier ($\Delta E(S) > \Delta E(SO) > \Delta E(C)$). This result suggests that in our system, the barrier is not the dominant factor governing the contact resistivity. Xie *et al.* [36–38] systematically studied the factors governing tunneling resistance in molecular junctions, and proposed a single-level model to explain the phenomenon. Their work demonstrates that interfacial contact resistance primarily depends on the coupling strength between ferromagnetic electrode and organic molecules; the stronger the coupling, the lower would be the interfacial contact resistance. Figure 3(b) depicts the spatial distribution of the HOMO of S12 throughout the molecular framework, along with the HOMO of SO12 concentrated at the end of the alkyl chain and that of C12 concentrated at opposite molecular ends (the anchoring group). Therefore, the spatial distributions of the HOMOs in C12 and SO12 are localized farther from the ends of the molecules and may cause weaker contact coupling at the interface. Therefore, the spatial distributions of the HOMOs in C12 and SO12 are localized farther from the ends of the molecules and may cause weaker contact coupling at the interface. The spatial distributions of HOMO in the three categories of molecule (n = 4, 8, or 16/18) exhibit similar localization. Consequently, the contact resistivity of S(Sn) is significantly lower than those of S(Cn) and S(SOn), resulting in reduced resistivity for S(Sn) as well. As discussed below, the adsorption energy and bond strength derived from theoretical simulations can quantitatively confirm the coupling strength between Fe_3O_4 and the molecules. Strong interfacial coupling effectively reduces the contact resistivity and enhances carrier transport [32]. Thus, selecting an appropriate anchor

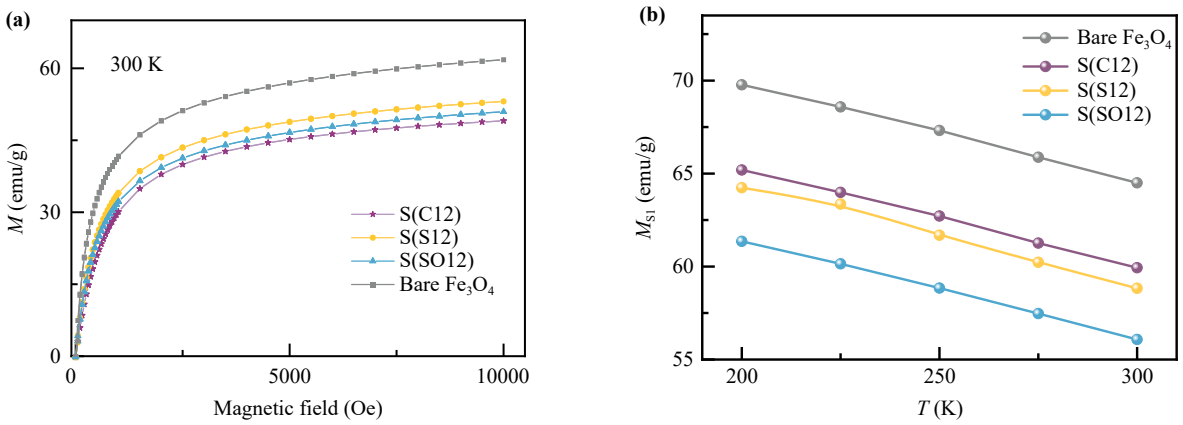

Fig. 4 **(a)** Magnetization curves of S(C12), S(S12), S(SO12), and bare Fe_3O_4 at 300 K. **(b)** M_{S1} vs. T for S(C12), S(S12), S(SO12), and bare Fe_3O_4 at 1 T.

group is the most direct and effective strategy for modulating carrier transport at the ferromagnet/molecule interface in device design.

3.2 Spin-dependent properties at Fe_3O_4/molecule interface

In addition to electrical transport, we examined the influence of anchoring groups on the magnetic properties and spin transport of the samples. Figure 4(a) shows the magnetization curves of S(C12), S(S12), S(SO12), and bare Fe_3O_4 at 300 K, all of which exhibit superparamagnetic behavior. The saturation magnetization (M_S) of bare Fe_3O_4 was 61.8 emu/g at 1 T, whereas M_S decreased for Fe_3O_4 coated with molecules. As demonstrated below, this reduction can be attributed to two primary factors. First, the mass fraction of organic molecules and residual moisture in the sample contribute to this reduction. To exclude the molecular mass contribution, thermogravimetric analysis (TGA) was conducted on these four samples. The S(C12), S(S12), S(SO12), and bare Fe_3O_4 fine powder samples were gradually heated from 30 °C to 600 °C at a rate of 5 °C/min in a high-purity nitrogen (99%) atmosphere respectively. The results indicated that the contents of organic molecules and moisture in the sample led to low saturation magnetization (M_S) (Table 2).

After excluding this effect, the intrinsic saturation magnetization (M_{S1}) of Fe_3O_4 in the four samples is shown in Fig. 4(b), M_{S1} for bare Fe_3O_4 remains higher than that of the coated samples, indicating that other factors also contribute. Secondly, surface modification of Fe_3O_4 nanoparticles by the coated molecules induces interfacial orbital hybridization, which modifies the surface magnetic moment and consequently influences the nanoparticle's saturation magnetization [39]. A similar effect has been observed when surfactants were coated on Fe_3O_4 nanoparticles [40]. The order $M_{S1}(Fe_3O_4) > M_{S1}(C12) > M_{S1}(S12) > M_{S1}(SO12)$ demonstrated that altering the anchoring groups can effectively tune the magnetic properties of the Fe_3O_4 nanoparticle surface.

To thoroughly analyze the variation in the magnetic moment on the Fe_3O_4 surface upon molecular adsorption, theoretical studies based on DFT were conducted. For the adsorption model, Fe_3O_4 slabs with saturated adsorption of –COOH, $–SO_3H$, and $–OSO_3H$ groups were constructed for simulations [Figs. 5(a)–(c)], where the O atoms of the adsorbates form bonds with Fe atoms to stabilize the adsorption structure. Analysis of the magnetic moment distribution reveals that the Fe atoms involved in the adsorption exhibit an opposite spin state compared to those in pure Fe_3O_4 [Figs. 6(a), (c), (e)]. These results indicate that molecular adsorption induces an antiparallel spin arrangement of Fe atoms, thereby reducing the total magnetic moment of Fe_3O_4. This

Table 2 Comparison of the saturation magnetization of different samples.

Sample	Bare Fe_3O_4	S(C12)	S(S12)	S(SO12)
M_S(1T)	61.8 emu/g	49.1 emu/g	53.1 emu/g	51.0 emu/g
Moisture	4.20%	2.30%	1.73%	1.82%
Molecules		15.75%	7.97%	7.28%
Fe_3O_4	95.80%	81.95%	90.30%	90.90%
M_{S1}(1T)	64.5 emu/g	59.9 emu/g	58.8 emu/g	56.1 emu/g

Note: M_S is the magnetization of the sample; M_{S1} is the intrinsic magnetization of the Fe_3O_4 core, calculated by subtracting the mass fraction of molecules and moisture.

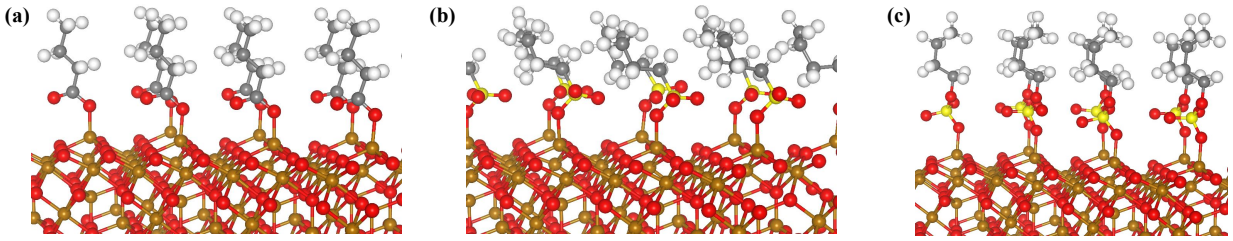

Fig. 5 Adsorption model of –COOH **(a)**, –SO_3H **(b)**, and –OSO_3H **(c)** on Fe_3O_4 (111). The gray, red, yellow, white, and brown balls denote the C, O, S, H, and Fe atoms, respectively.

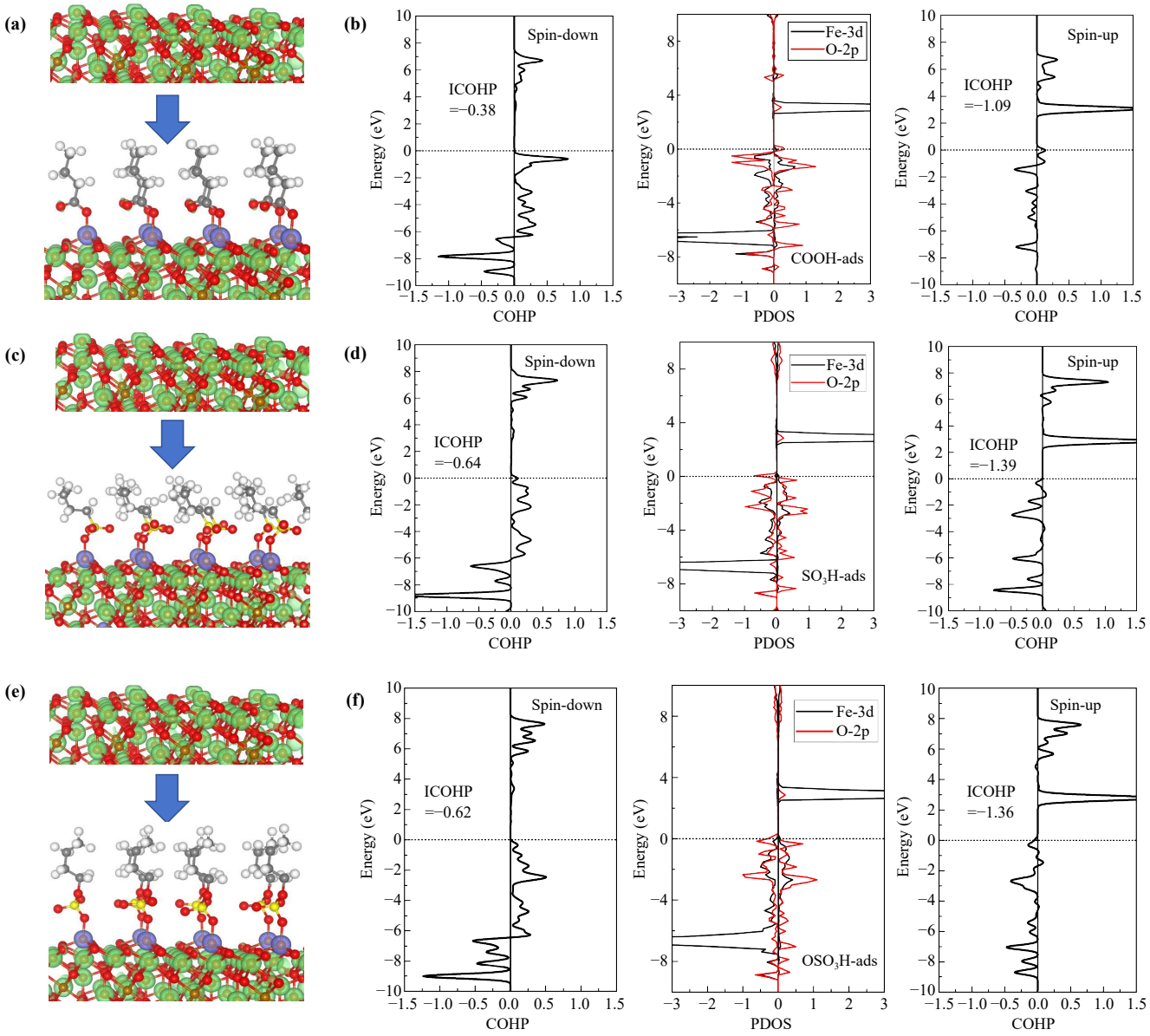

Fig. 6 **(a)** Change in the spin polarization direction of Fe_3O_4 after C4 adsorption. The green and blue areas represent different magnetic moment directions (spin polarization directions). The same convention is applied to S4 **(c)** and SO4 **(e)**. The electronic structures of Fe–O in Fe_3O_4–COOH **(b)**, Fe_3O_4–SO_3H **(d)**, and Fe_3O_4–OSO_3H **(f)**.

theoretical finding is in good agreement with our experimental results.

To further elucidate the underlying mechanism of this phenomenon, electronic structures, including partial

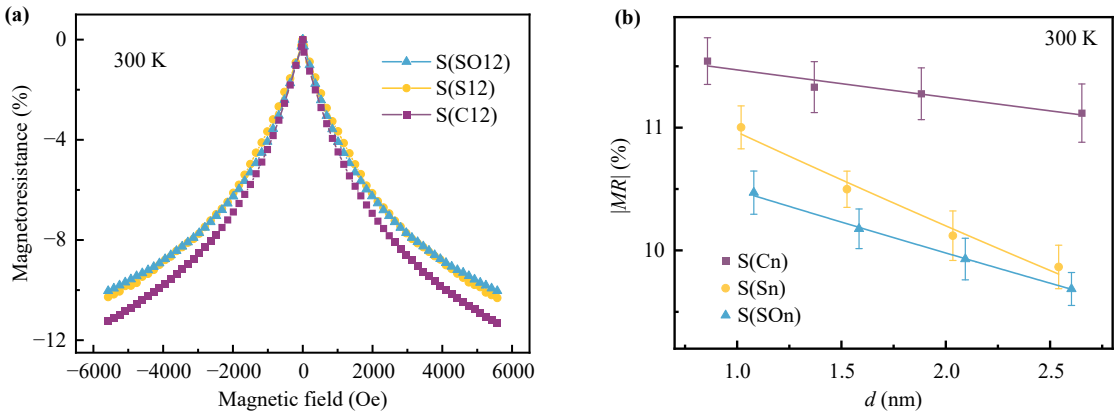

Fig. 7 **(a)** Magnetoresistance curves for S(C12), S(S12), and S(SO12) at 300 K. **(b)** Dependence of *MR* as a function of molecular length *d* at 300 K.

density of states (PDOS), crystal orbital Hamilton population (COHP), and differential charge density, were systematically investigated. The PDOS analysis in Fig. 6(b) reveals that the Fe-3*d* orbitals strongly hybridize with the O-2*p* orbitals of C4, forming Fe–O bonds that facilitate adsorption. The COHP results further confirm that the spin-up channel is the major contributor to the Fe–O bond, as evidenced by a higher integrated COHP (ICOHP) value (–1.09) compared to that of the spin-down channel (–0.38). As shown in Figs. 6(d) and (f), the same phenomenon is observed in the $–SO_3H$ and $–OSO_3H$ systems, where the spin-up channel primarily contributes to Fe–O bonding. The ICOHP values follow the order: $–SO_3H$ (–1.39) < $–OSO_3H$ (–1.36) < –COOH (–1.09), the more negative ICOHP values of $–SO_3H$ and $–OSO_3H$ indicate stronger hybridization between the Fe-3*d* and O-2*p* orbitals, as reflected in adsorption energy. Specifically, the DFT results show that $–SO_3H$ exhibits the strongest adsorption, with an adsorption energy (ΔE_{ads}) of –5.22 eV/molecule, followed by $–OSO_3H$ (ΔE_{ads} = –4.51 eV/molecule) and –COOH (ΔE_{ads} = –4.09 eV/molecule). The stronger the adsorption or bonding, the greater the interface coupling, which possibly quantitatively explain the interface coupling we mentioned earlier.

A comprehensive analysis suggests that the differences in the saturation magnetization (M_{S1}) among the three samples [Fig. 4(b)] may be attributed to the chemical bonding strength (ICOHP) and the charge transfer at the Fe_3O_4/molecule interface. As discussed before, strong interfacial bonding ($–SO_3H$/$–OSO_3H$) induces severe *p*–*d* orbital hybridization, in which spin-up electrons participate in the formation of interfacial Fe–O bonds. Unlike the surface spin-down electrons, these bonding spin-up electrons are effectively 'pinned' due to the strong orbital interaction. This asymmetric spin involvement disrupts the intrinsic super-exchange interactions in Fe_3O_4 as well as might rigidly lock the surface Fe spins into a magnetically inactive or antiparallel configuration, thereby impeding their alignment with the external magnetic field [39, 41]. In contrast, weaker bonding (–COOH) likely imposes relatively fewer constraints on the surface spins, thereby posing fewer obstacles to their alignment with the magnetic field, as discussed in Part 5 of the Electronic Supplementary Materials. Furthermore, charge transfer at the Fe_3O_4/molecule interface further modifies the saturation magnetization (M_{S1}) of these samples. UPS analysis revealed a significant increase in the work function for all samples, indicating charge transfer from Fe_3O_4 to the absorbed molecules, this phenomenon was further supported by theoretical calculations (Part 4 of the Electronic Supplementary Materials). This charge transfer could induce Fe^{2+} oxidation and reduce the interfacial Fe^{2+}/Fe^{3+} ratio, thereby lowering the magnetization. Although S(C12) exhibited a slightly larger increase in work function, probably suggesting a more pronounced interfacial charge transfer [42], its significantly weaker "pinning" allows a greater portion of the surface spins to remain responsive to the external magnetic field compared to S(S12) and S(SO12). Ultimately, the saturation magnetization of the samples is codetermined by these two factors.

3.3 Magneto-transport

We investigated the role of anchoring groups in the magneto-transport of the samples. Figure 7(a) shows the magnetoresistance curves of S(C12), S(S12), and S(SO12) at 300 K. Under an applied magnetic field of 5500 Oe, the magnetoresistance (*MR*) values for these samples were –11.25%, –10.28%, and –10.04%, respectively. The *MR* decreased monotonically with increasing magnetic field — a trend that contrasted with the magnetization curve, which approached saturation at 2 kOe. This discrepancy indicates that both the bulk magnetic moment of Fe_3O_4 particles and their surface magnetic moment play critical roles in spin transport.

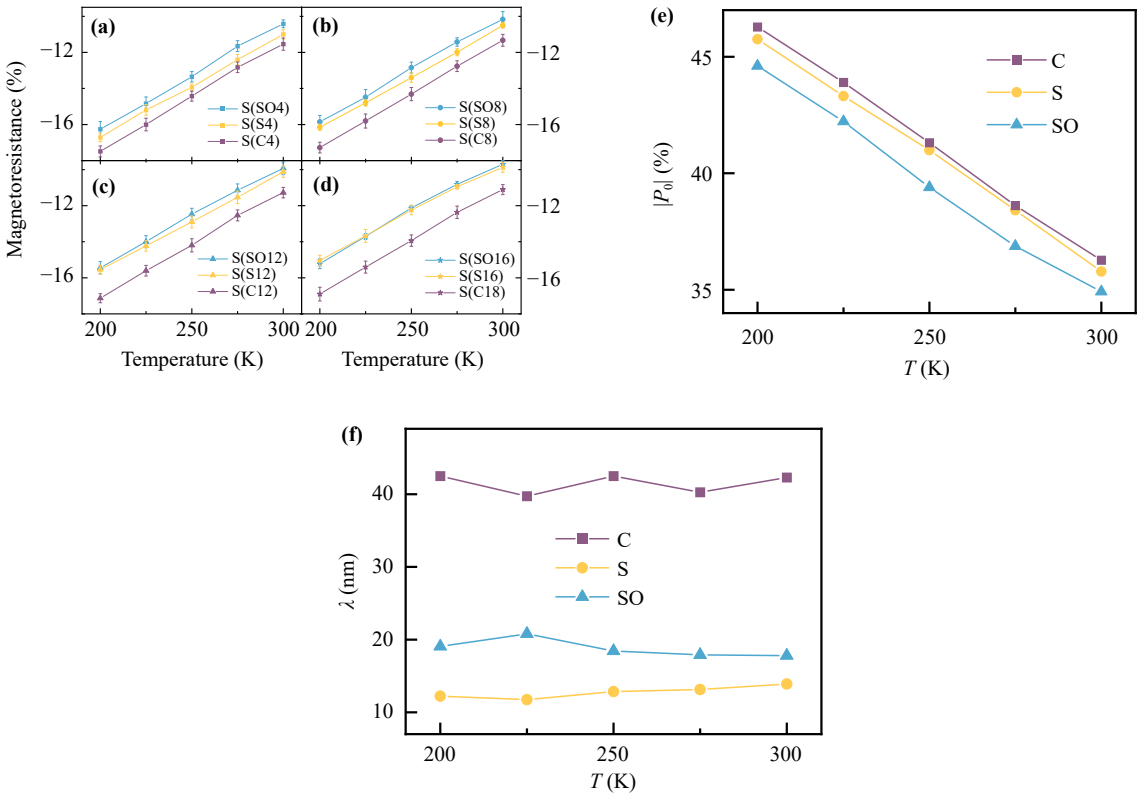

Fig. 8 **(a–d)** *MR* vs. T for S(Sn), S(Cn), and S(SOn) at 5.5 kOe. **(e)** $|P_0|$ vs. T and **(f)** λ vs. T for S(Sn), S(Cn), and S(SOn) at 5.5 kOe.

Furthermore, the differences in *MR* among the samples suggested that magneto transport is regulated by the anchoring groups.

Figure 7(b) presents the *MR*–d curves at 300 K, showing that *MR* decayed exponentially as the molecular length (d) increased. The decay rate varied with the anchoring group: *MR* decayed most slowly for carboxylic acid samples, followed by sulfuric acid samples, and most rapidly for sulfonic acid samples. When the spin polarization of interface-injected carriers was P_0, it decayed to $P_0 \cdot e^{-d/\lambda}$ after tunneling through the molecular layer, where λ was the spin diffusion length. According to the Jullière model, *MR* can be expressed as [43]

$$|MR| = \left|\frac{R(H) - R(0)}{R(0)}\right| = \frac{P_0^2 e^{-d/\lambda}}{1 + P_0^2 e^{-d/\lambda}}, \quad (1)$$

where $R(H)$ and $R(0)$ denote the resistance under an applied magnetic field H and under zero magnetic field, respectively. The Jullière model assumes ideal spin injection and negligible interfacial spin scattering. In our system, considering the influence of orbital hybridization, P_0 refers to the spin polarization of the injected carriers, which not only reflects the intrinsic spin polarization of Fe_3O_4, but also includes the effect of different anchoring groups on interfacial spin injection. Xiong *et al.* [43] used the same method to fit the spin diffusion length in LSMO/Alq_3/Co devices. The *MR*–d data for these samples were fitted using Eq. (1), yielding λ_C (300 K) = 42.3 nm, λ_{SO} (300 K) = 17.8 nm, and λ_S (300 K) = 13.2 nm, with the relationship $\lambda_C > \lambda_{SO} > \lambda_S$.

As shown in Figs. 8(a)–(d), the temperature-dependent tunneling magnetoresistance (*MR*) is plotted for S(Cn), S(Sn), and S(SOn). The *MR* values decreased linearly with decreasing temperature (T), independent of the type and length of the coated molecules, the nearly identical slopes are likely due to the common constituent material of these samples — Fe_3O_4. Figure 8(e) shows that $|P_0|$ increased with decreasing T. Previous studies have indicated that spin polarization is related to the saturation magnetization [44, 45], and the same slopes is also observed in the M_{S1}–T curves of the samples [Fig. 4(b)]. M_{S1} decreased monotonically with increasing T for all three coated samples. Moreover, the order of M_{S1} is M_{S1}(C12) > M_{S1}(S12) > M_{S1}(SO12), which matches the order of $|P_0(C)| > |P_0(S)| > |P_0(SO)|$. As discussed earlier, the anchoring groups alter the surface magnetic moment of Fe_3O_4 nanoparticles via p–d orbital hybridization and charge transfer, consequently leading to a change in the intrinsic spin polarization of Fe_3O_4. Because most electrons participating in tunneling transport originate from the particle surface, the surface magnetic moment plays a dominant role in spin transport.

Additionally, orbital hybridization at the

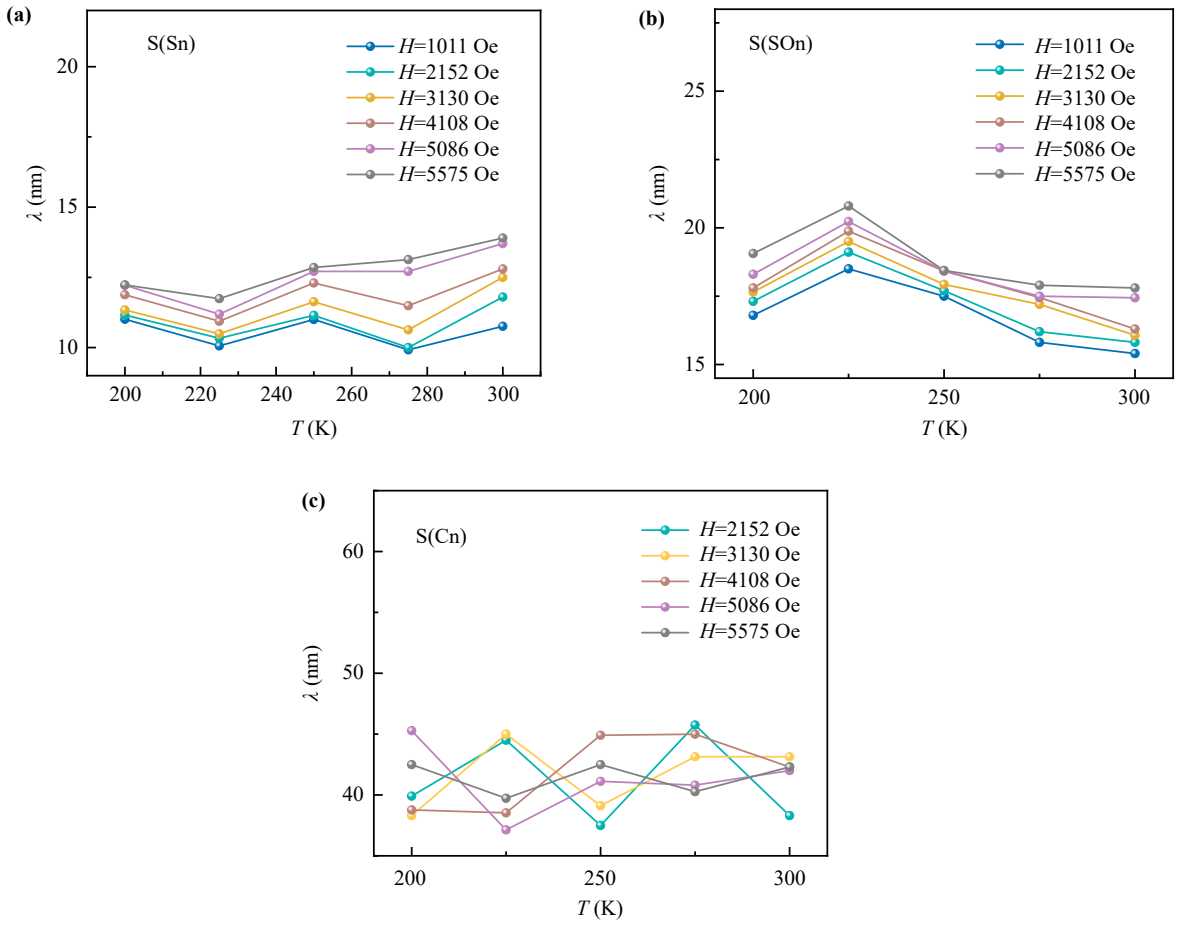

Fig. 9 **(a)** λ vs. T in sulfonic acid. **(b)** λ vs. T in sulfuric acid. **(c)** λ vs. T in carboxylic acid.

Fe_3O_4/molecule interface also influences the spin injection. As evidenced by the ICOHP and PDOS results in Fig. 6, for the spin-up channel, a clear energy gap between the bonding and anti-bonding states is observed across all samples, effectively acting as an additional tunneling barrier. In contrast, the ICOHP values in the spin-down channel are close to zero, specifically –0.62 for $–SO_3H$, –0.60 for $–OSO_3H$, and –0.38 for –COOH, indicating weak Fe-O interactions. Meanwhile, for the ICOHP of Fe-O in the spin-down channel, the anti-bonding states are occupied by electrons below the Fermi level, thus it providing a preferential tunneling pathway for spin-down carrier, this is applicable to all samples.

As illustrated in Fig. 8(a), for $n = 4$, $|MR(\mathrm{C4})| > |MR(\mathrm{S4})| > |MR(\mathrm{SO4})|$. With increasing molecular length (d), the MR–T curve of S(Sn) gradually approached that of S(SOn) [Figs. 8(b) and (c)], whereas the difference between these two curves and that of S(Cn) became increasingly pronounced. At $n = 16$, the MR curves of S(S16) and S(SO16) nearly overlapped [Fig. 8(d)], differing by approximately 1.3% from S(C18). These observations indicated that MR decayed with d at different rates across the three categories sample, implying that their spin diffusion lengths (λ) differed.

Figure 8(f) shows λ as a function of temperature (T) in the range 150–300 K. Interestingly, λ is T-independent, indicating that the decrease in MR with T was not caused by intramolecular spin relaxation. A similar T-independent λ was reported by Jiang *et al.* [46], who studied exchange interaction-dominated spin current transport through Alq_3 molecules in $Y_3Fe_5O_{12}/Alq_3/Pd$ heterostructures. At 5.5 kOe, the intramolecular spin diffusion lengths for sulfonic acid, sulfuric acid, and carboxylic acid were $\lambda_S = 12.8 \pm 0.8$ nm, $\lambda_{SO} = 18.1 \pm 0.7$ nm, and $\lambda_C = 41.5 \pm 1.3$ nm, respectively. These results demonstrate that –COOH provides superior spin injection efficiency and transport properties at the Fe_3O_4/molecule interface compared with other anchoring groups.

Therefore, we examined whether the T-independent properties of λ persisted under different magnetic fields. Figures 9(a), (b), and (c) list the λ–T curves of sulfonic acid, sulfuric acid, and carboxylic acid samples at different magnetic fields, respectively. Notably, λ remained essentially T-independent across all measured fields, indicating that phonon scattering exerted a negligible influence on

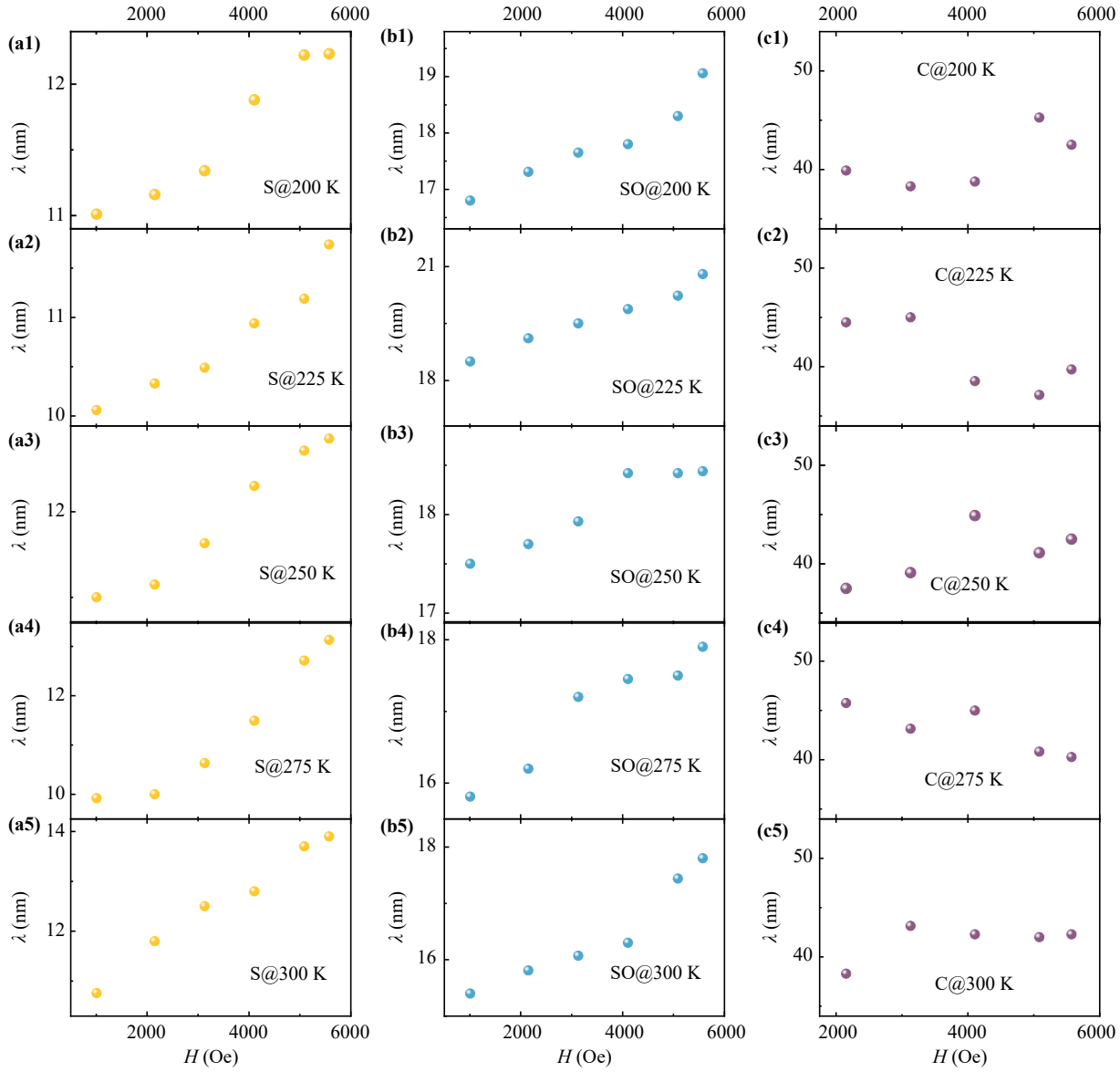

Fig. 10 Dependence of intramolecular spin diffusion length (λ) on external magnetic field (H) in sulfonic acid (S) **(a1–a5)**, sulfuric acid (SO) **(b1–b5)**, and carboxylic acid (C) **(c1–c5)** within 200–300 K.

spin relaxation during tunneling transport. This behavior contrasted sharply with temperature-dependent spin relaxation mechanisms observed in carrier hopping [47], where spin relaxation was predominantly governed by spin–orbit coupling (SOC) [26] or hyperfine interactions (HFI) [48]. Due to the T-dependent hopping rate, the spin diffusion length in the HFI-dominated spin relaxation increase with T. For SOC-dominated hopping transport, λ decreases with increasing T. Therefore, the disparate T-dependences between SOC- and HFI-induced spin relaxation allow an experimental determination of spin relaxation mechanisms in individual organic solids. However, in our study, it was the intramolecular tunneling between Fe_3O_4 particles that was nearly T-independent; thus, spin relaxation caused by SOC or HFI was similarly unaffected by temperature. Although the electron density near the fermi level of Fe_3O_4 increased with T, this primarily influenced the number of carriers participating in tunneling [49], rather than the barrier height, width, or tunneling probability.

We further investigated the effect of applied magnetic fields (H) on spin relaxation in organic molecules. As shown in Fig. 10, λ_S and λ_{SO} increased monotonically with H in the range of 200–300 K. Specifically, λs increased by 1.2–3.2 nm, whereas λ_{SO} increased by 1.9–2.4 nm. Then whether this change related to a non-intrinsic effect associated with differences in magnetic interactions between adjacent Fe_3O_4 particles? Specifically, to stabilize the system, the magnetic moments of adjacent Fe_3O_4 particles tend to be antiparallel, exhibiting

a certain degree of anti-ferromagnetism. Compared to S(S16), S(S4) exhibits stronger inter-particle magnetic interactions and a more significant resistivity increase due to its shorter molecule length. When a magnetic field was applied, the magnetic moments gradually aligned with the field direction, increasing $|\rho(H)–\rho(0)|$ and consequently enhancing *MR* in the absence of inter-particle magnetic interactions. Then, as *d* increased and the distance between adjacent Fe_3O_4 nanoparticles grew, both the magnetic interaction and the resistivity $\rho(0)$ changed — the former decayed, and the latter increased — thereby reducing the net contribution to $|\rho(H)–\rho(0)|$. Thus, long-chain molecular samples exhibited smaller *MR* changes than short-chain counterparts, leading to shorter λ. With increasing *H*, $|\rho(H)–\rho(0)|$ continued to grow, whereas the contribution from magnetic interactions to $|\rho(H)–\rho(0)|$ and *MR* became progressively weaker; thus, λ obtained from *MR*–*d* fitting increased with *H*.

However, Rackham *et al.* [50] reported magnetic ordering of nanospins in the system of oleic acid-coated 11 nm Fe_3O_4 particles. The concentrations ferromagnetism and magnetic random nanospins exceed that of anti-ferromagnetism. When $H > 1000$ Oe, the antiferromagnetic concentration of nanospins tends to saturate and remains constant; similarly, the concentration of ferro-magnetic and random nanospins also essentially saturates at ~3000 Oe [50]. Physically, this magnetic interaction defines a finite energy scale for spin alignment; once the external magnetic field overcomes this energy and stabilizes the interparticle magnetic configurations, the non-intrinsic spin scattering arising from magnetic mismatch should reach a limit. For instance, based on the derived magnetic moment μ of per Fe_3O_4 nanoparticle from Table 2 and considering the molecular length *d* of S12, the estimated interparticle magnetic interaction energy $E_{dip} \sim \mu^2/r^3$ for S(S12) is approximately 1.47×10^{-21} J at 300 K. This energy corresponds to an effective magnetic field of ~91.8 Oe, which is ~0.35 times the thermal energy ($k_B T$) and considerably lower than the Zeeman energy ($E_{zee} \sim \mu H = 1.60\times10^{-20}$ J) of Fe_3O_4 particles at 1000 Oe. Therefore, the magnetic interaction is likely more than 10 times lower than the Zeeman energy. If our observed λ–*H* is solely governed by the magnetic dipole interactions, then its curve should likewise plateau alongside the magnetic ordering. Instead, λ increases continuously up to 5500 Oe (Fig. 10), diverging significantly from the saturation of antiferromagnetic and ferromagnetic concentration. Moreover, magnetic interactions are *T*-dependent, which contradicts the *T*-independent λ (Fig. 9).

During tunneling transport, external magnetic field-induced energy splitting occurs between the spin-up and spin-down electrons — known as the Zeeman effect. The induced energy difference ($\Delta E = \mu_B g H$) could suppress the spin-flip scattering caused by SOC during tunneling. With increasing *H*, ΔE increases, further lowering the spin-flip probability and resulting in an increased λ despite the presence of thermal disturbances. Such thermal disturbances mainly affect the magnetic order on the surface of the Fe_3O_4 particles rather than affecting the spin relaxation during tunneling, as tunneling is temperature-independent, which is demonstrated by the results shown in Fig. 9. Therefore, this result strongly suggests that the Zeeman effect serves as the principal mechanism for the variation of λ with *H* [Figs. 10(a1)–(a5) and Figs. 10(b1)–(b5)]. However, this trend is not observed in the carboxylic acid molecules [Figs. 10(c1)–(c5)]. In this case, λ does not show a distinct monotonic dependence on *H*. This is likely because the carriers experience weaker SOC during tunneling through these molecules —as evidenced by the significantly higher λ and discussed further below—resulting in an extremely low probability of spin flipping. Consequently, the influence of the magnetic field on λ is not significant, and distinguishing it within the experimental error range is challenging.

Most importantly, the magnetic field modulated λ within a range of 1–3 nm, which was smaller than the minimum difference of ~ 6 nm between any two of the three sample categories. Consequently, the relationship $\lambda_C > \lambda_{SO} > \lambda_S$ still existed, with $\lambda_C/\lambda_S \approx 3.2$ and $\lambda_C/\lambda_{SO} \sim 2.3$, indicating that replacing the carbon-centered anchoring group (–COOH) with sulfur-centered groups (–SO_3H, –OSO_3H) enhanced intramolecular spin relaxation during tunneling. In organic semiconductors, SOC or HFI is the primary cause of spin relaxation [51]. For molecules studied in this work, HFI was primarily governed by atoms with half-integer spins, such as H atoms. In all three molecular categories, the H atoms were located along the alkyl chains, and their numbers were comparable. The effective magnetic field generated by HFI was estimated to be on the order of tens of Oe — two orders of magnitude smaller than the applied magnetic field (typically several kOe) — and thus could not account for a more than threefold difference in spin diffusion length. Moreover, HFI became increasingly suppressed at higher magnetic fields [48], confirming that it was not the primary cause of spin relaxation.

SOC is a critical factor governing spin relaxation in molecules and is influenced by different parameters such as atomic number (*Z*) [52], molecular structure [11], and other intrinsic properties. In organic molecules, the SOC strength typically scales with the fourth power of the atomic number (Z^4) [53]. For the molecules examined in this study, differences in the central atoms of the anchoring groups could affect SOC, potentially explaining the trend $\lambda_C > \lambda_S$. However, the λ_C/λ_S ratio (~3.2) deviates substantially from the theoretical $Z^4(S)/Z^4(C)$ ratio, and the fact that $\lambda_{SO} > \lambda_S$ indicated that inserting oxygen atoms into the anchoring group (–SO_3H) increased λ. This finding suggests that, beyond heavy-atom-induced SOC, additional mechanisms influence spin relaxation,

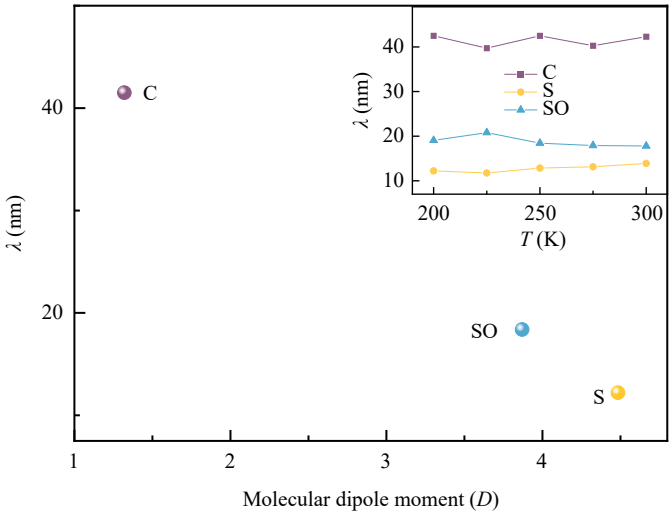

Fig. 11 Plot of λ *vs.* molecular dipole moment at 5.5 kOe.

possibly related to SOC arising from intrinsic molecular dipole moments. We investigated the correlation between λ and molecular dipole moment across the three sample categories, as shown in Fig. 11, and found that smaller dipole moments corresponded to larger λ values. This behavior was likely attributed to the intrinsic dipole moment generating non-uniform local electric fields within the molecule, which disrupted the system's structural inversion symmetry and modulated SOC during tunneling. A larger dipole moment probably produces a steeper electric field gradient, enhancing the SOC effect [54], increasing spin scattering, and thereby reducing the spin diffusion length [55, 56]. Additionally, dipole moments could also alter the SOC strength by modifying the intramolecular charge distribution. As mentioned earlier, chemical adsorption induces charge transfer at the Fe_3O_4/molecule interface, where electrons are transferred from Fe_3O_4 to the adsorbed molecules (Part 4 of the Supplementary Materials). This process leads to a high electron density around the oxygen atoms, resulting in the formation of localized charge centers. Such an inhomogeneous charge distribution enhances the intramolecular local electric-field gradient, thereby influencing the SOC. Further studies are necessary to fully elucidate the detailed spin relaxation mechanisms during tunneling.

4 Conclusions

In summary, we fabricated Fe_3O_4/carboxylic acid, Fe_3O_4/sulfonic acid, and Fe_3O_4/sulfuric acid hybrid nanoparticles to experimentally and theoretically investigate the effects of anchoring atoms (S and C) on spin transport at the Fe_3O_4/molecule interface, spin relaxation, and the underlying physical mechanisms. Electrical transport measurements revealed that the contact resistivity at the Fe_3O_4/molecule interface was highly sensitive to the anchoring groups, following the trend ρ_c(–COOH) > ρ_c(–OSO_3H) > ρ_c(–SO_3H). The theoretical calculations indicated that this behavior was primarily determined by the coupling strength between Fe_3O_4 and the molecules. Magneto-transport results further demonstrated that replacing the carbon-centered anchoring group (–COOH) with sulfur-centered groups (–SO_3H, –OSO_3H) reduced the magnetoresistance and decreased the spin diffusion length (λ) by approximately 69%. DFT calculations were performed to clarify the role of orbital hybridization in tuning the interfacial magnetic properties and spin transport. An analysis of λ using the Jullière model allowed us to examine its dependence on magnetic field and temperature, revealing that the temperature-independent behavior of λ originated from tunneling transport, while its field-dependent behavior stemmed from the Zeeman effect. Our findings strongly suggest that the SOC induced by the dipole moments of the molecules is the dominant factor governing the observed variations in spin relaxation during tunneling. This work provides the first experimental verification of spin scattering within an organic molecule during tunneling and demonstrates the feasibility of controlling spin injection and transport by altering the central atom of the anchoring group, offering new strategies for actively tuning spin transport at ferromagnet/molecule interfaces on the molecular scale.

Declarations The authors declare that they have no competing interests and there are no conflicts.

Data availability The data that support the findings of this study are available from the corresponding author upon reasonable request.

Electronic supplementary materials It mainly includes six parts of discussion: i) All isolated molecular energy levels; ii) Carrier transport mechanisms: tunneling; iii) Computational details and model; iv) Charge transfer at the Fe_3O_4/molecule interface; v) Effect of surface modification on magnetic properties; vi) The rationality for extending the carboxylic acid series to C18. See: https://doi.org/10.15302/frontphys.2026.055203.

Acknowledgements This work was supported by the Key Research and Development Project of High-Level Scientific and Technological Talent Introduction for Lyuliang City (Grant Nos. 2023RC18 and 2023RC10), the National Natural Science Foundation of China (Grant No. 11404197), the Natural Science Foundation of Shanxi Province (Grant No. 202503021211086), and the Natural Science Foundation of Jilin Province (No. 20250102105JC). The computational time is also supported by the computing center of Jilin Province.

References

1. B. Liu, X. Zhang, J. Xiong, X. Pang, S. Liu, Z. Yang, Q. Yu, H. Li, S. Zhu, and J. Wu, Spin transport of half-

metal Mn2X3 with high Curie temperature: An ideal giant magnetoresistance device from electrical and thermal drives, *Front. Phys. (Beijing)* 19(4), 43201 (2024)
2. M. S. Ansari, M. O. Ansari, S. Ansari, M. S. Abdelwahab, and S. A. Ansari, Defect-engineered spintronic functionality via F-center exchange in quantum-confined ZnO/CuO heterostructures, *Ceram. Int.* 51(30), 65333 (2025)
3. M. G. Alam, S. Ansari, and M. S. Ansari, Defect-engineered room-temperature ferromagnetism in Fe, Ni Co-doped CuO hierarchical nanostructures for advanced spintronics, *Ceram. Int.* 51(25), 45188 (2025)
4. G. Li, F. Xu, and J. Wang, Universal behaviors of magnon-mediated spin transport in disordered nonmagnetic metal-ferromagnetic insulator heterostructures, *Front. Phys. (Beijing)* 18(3), 33310 (2023)
5. L. J. Qian, L. Duan, X. W. Jin, and Z. Y. Yang, Spintronic timing switches via magnetic breather oscillations, *Front. Phys. (Beijing)* 21(6), 065202 (2026)
6. M. S. Ansari, M. H. D. Othman, M. O. Ansari, S. Ansari, and H. Abdullah, Progress in Fe_3O_4-centered spintronic systems: Development, architecture, and features, *Appl. Mater. Today* 25, 101181 (2021)
7. M. S. Ansari, M. H. D. Othman, M. O. Ansari, S. Ansari, H. Abdullah, and Z. Harun, Magnetite thin films grown on different flexible polymer substrates at room temperature: Role of antiphase boundaries in electrical and magnetic properties, *J. Alloys Compd.* 846, 156368 (2020)
8. M. S. Ansari, M. H. D. Othman, M. O. Ansari, S. Ansari, and N. Sazali, Large spin-dependent tunneling magnetoresistance in Fe_3O_4/PET heterostructures developed at room temperature: A promising candidate for flexible and wearable spintronics, *Mater. Sci. Eng. B* 265, 115033 (2021)
9. M. S. Ansari, M. H. D. Othman, M. O. Ansari, S. Ansari, and H. Abdullah, Reactively sputtered half-metallic Fe3O4 thin films at room temperature on polymethyl methacrylate: A perspective for flexible spintronics, *Ceram. Int.* 46(11), 19302 (2020)
10. M. S. Ansari, M. H. D. Othman, M. O. Ansari, S. Ansari, and M. Z. M. Yusop, Room temperature growth of half-metallic Fe_3O_4 thin films on polycarbonate by reactive sputtering: Heterostructures for flexible spintronics, *J. Alloys Compd.* 816, 152532 (2020)
11. T. Yang, Y. Qin, M. Wu, L. Guo, X. Gu, K. Meng, S. Hu, C. Zhang, R. Zheng, R. Zhang, and X. Sun, Structural isomeric effect on spin transport in molecular semiconductors, *Adv. Mater.* 36(26), 2402001 (2024)
12. K. Meng, L. Guo, and X. Sun, Strategies and applications of generating spin polarization in organic semiconductors, *Nanoscale Horiz.* 8(9), 1132 (2023)
13. V. A. Dediu, L. E. Hueso, I. Bergenti, and C. Taliani, Spin routes in organic semiconductors, *Nat. Mater.* 8(9), 707 (2009)
14. S. Hu, Y. Qin, S. Lu, L. Guo, X. Gu, T. Yang, R. Zhang, K. Meng, C. Zhang, M. Wu, and X. Sun, Interface engineering for enhancing air-stable spin-charge interaction in molecular spin-photovoltaic devices, *Adv. Funct. Mater.* 34(23), 2315239 (2024)
15. S. Delprat, M. Galbiati, S. Tatay, B. Quinard, C. Barraud, F. Petroff, P. Seneor, and R. Mattana, Molecular spintronics: the role of spin-dependent hybridization, *J. Phys. D Appl. Phys.* 51(47), 473001 (2018)
16. A. Bedoya-Pinto, S. G. Miralles, S. Vélez, A. Atxabal, P. Gargiani, M. Valvidares, F. Casanova, E. Coronado, and L. E. Hueso, Interface-assisted sign inversion of magnetoresistance in spin valves based on novel lanthanide quinoline molecules, *Adv. Funct. Mater.* 28(16), 1702099 (2018)
17. M. Cinchetti, V. A. Dediu, and L. E. Hueso, Activating the molecular spinterface, *Nat. Mater.* 16(5), 507 (2017)
18. S. Sanvito, The rise of spinterface science, *Nat. Phys.* 6(8), 562 (2010)
19. A. Forment-Aliaga and E. Coronado, Hybrid interfaces in molecular spintronics, *Chem. Rec.* 18(7–8), 737 (2018)
20. L. Guo, S. Hu, X. Gu, R. Zhang, K. Wang, W. Yan, and X. Sun, Emerging spintronic materials and functionalities, *Adv. Mater.* 36(22), 2301854 (2024)
21. S. Qiu, Y. Y. Miao, G. P. Zhang, J. F. Ren, C. K. Wang, and G. C. Hu, Enhancement of magnetoresistance and current spin polarization in single-molecule junctions by manipulating the hybrid interface states via anchoring groups, *J. Magn. Magn. Mater.* 479, 247 (2019)
22. S. Shi, Z. Sun, A. Bedoya-Pinto, P. Graziosi, X. Li, X. Liu, L. Hueso, V. A. Dediu, Y. Luo, and M. Fahlman, Hybrid interface states and spin polarization at ferromagnetic metal–organic heterojunctions: Interface engineering for efficient spin injection in organic spintronics, *Adv. Funct. Mater.* 24(30), 4812 (2014)
23. Z. Zhang, S. Qiu, Y. Miao, J. Ren, C. Wang, and G. Hu, Spin selection at organic spinterface by anchoring group, *Appl. Surf. Sci.* 409, 60 (2017)
24. S. Qiu, Y. Y. Miao, G. P. Zhang, J. F. Ren, C. K. Wang, and G. C. Hu, Modulation of hybrid interface states and magnetoresistance in quantum interference systems via functional groups, *J. Magn. Magn. Mater.* 537, 168138 (2021)
25. J. J. Li, Z. B. Chen, Y. H. Wang, X. S. Zhou, L. Q. Xie, Z. Shi, J. X. Liu, J. W. Yan, and B. W. Mao, Single-molecule anisotropic magnetoresistance at room temperature: Influence of molecular structure, *Electrochim. Acta* 389, 138760 (2021)
26. Z. G. Yu, Spin–orbit coupling, spin relaxation, and spin diffusion in organic solids, *Phys. Rev. Lett.* 106(10), 106602 (2011)
27. N. J. Harmon and M. E. Flatté, Distinguishing spin relaxation mechanisms in organic semiconductors, *Phys. Rev. Lett.* 110(17), 176602 (2013)
28. X. Shi, S. Wang, X. Su, Y. Shi, B. Shi, H. Zhou, and H. Jiao, Interfacial oxidation for spin transport in Fe_3O_4/sulfonic acid molecule nanoparticles, *Solid-State Electron.* 177(47), 107962 (2021)
29. S. Wang, F. J. Yue, J. Shi, Y. J. Shi, A. Hu, Y. W. Du, and D. Wu, Room-temperature spin-dependent tunneling through molecules, *Appl. Phys. Lett.* 98(17), 172501 (2011)
30. S. Wang, F. J. Yue, D. Wu, F. M. Zhang, W. Zhong, and Y. W. Du, Enhanced magnetoresistance in self-assembled monolayer of oleic acid molecules on Fe_3O_4 nanoparticles, *Appl. Phys. Lett.* 94(1), 012507 (2009)

31. X. Shi, F. Chen, S. Wang, Y. Shi, X. Su, H. Zhou, and H. Jiao, Enhancement of spin diffusion length in tunneling junctions by benzene ring insertion into the saturated alkyl sulfonic acid, *Appl. Phys. Express* 15(7), 073001 (2022)
32. L. A. Zotti, T. Kirchner, J. C. Cuevas, F. Pauly, T. Huhn, E. Scheer, and A. Erbe, Revealing the role of anchoring groups in the electrical conduction through single-molecule junctions, *Small* 6(14), 1529 (2010)
33. M. J. Frisch, G. W. Trucks, H. B. Schlegel, et al., Gaussian 16, Gaussian, Inc., Wallingford CT, 2016
34. A. D. Becke, Density-functional thermochemistry. I. The effect of the exchange-only gradient correction, *J. Chem. Phys.* 96(3), 2155 (1992)
35. R. Krishnan, J. S. Binkley, R. Seeger, and J. A. Pople, Self-consistent molecular orbital methods. XX. A basis set for correlated wave functions, *J. Chem. Phys.* 72(1), 650 (1980)
36. Z. Xie, I. Bâldea, C. E. Smith, Y. Wu, and C. Daniel Frisbie, Experimental and theoretical analysis of nanotransport in oligophenylene dithiol junctions as a function of molecular length and contact work function, *ACS Nano* 9(8), 8022 (2015)
37. Z. Xie, I. Bâldea, G. Haugstad, and C. Daniel Frisbie, Mechanical deformation distinguishes tunneling pathways in molecular junctions, *J. Am. Chem. Soc.* 141(1), 497 (2018)
38. Z. Xie, I. Bâldea, and C. Daniel Frisbie, Determination of energy-level alignment in molecular tunnel junctions by transport and spectroscopy: Self-consistency for the case of oligophenylene thiols and dithiols on Ag, Au, and Pt electrodes, *J. Am. Chem. Soc.* 141(8), 3670 (2019)
39. A. Mukhopadhyay, N. Joshi, K. Chattopadhyay, and G. De, A facile synthesis of PEG-coated magnetite (Fe_3O_4) nanoparticles and their prevention of the reduction of cytochrome C, *ACS Appl. Mater. Interfaces* 4(1), 142 (2012)
40. S. Arsalani, E. J. Guidelli, M. A. Silveira, C. E. G. Salmon, J. F. D. F. Araujo, A. C. Bruno, and O. Baffa, Magnetic Fe_3O_4 nanoparticles coated by natural rubber latex as MRI contrast agent, *J. Magn. Magn. Mater.* 475, 458 (2019)
41. R. Otani and H. Yao, Size and magnetic-field dependence of MCD spectra of magnetite (Fe_3O_4) nanoparticles synthesized by an L-proline-mediated solvothermal approach: Effect of surface spin disorder, *J. Phys. Chem. C Nanomater. Interfaces* 128(32), 13508 (2024)
42. P. Winget, L. K. Schirra, D. Cornil, H. Li, V. Coropceanu, P. F. Ndione, A. K. Sigdel, D. S. Ginley, J. J. Berry, J. Shim, H. Kim, B. Kippelen, J. L. Brédas, and O. L. Monti, Defect-driven interfacial electronic structures at an organic/metal-oxide semiconductor heterojunction, *Adv. Mater.* 26(27), 4711 (2014)
43. Z. H. Xiong, D. Wu, Z. Valy Vardeny, and J. Shi, Giant magnetoresistance in organic spin-valves, *Nature* 427(6977), 821 (2004)
44. A. H. MacDonald, T. Jungwirth, and M. Kasner, Temperature dependence of itinerant electron junction magnetoresistance, *Phys. Rev. Lett.* 81(3), 705 (1998)
45. J. S. Moodera, J. Nassar, and G. Mathon, Spin-tunneling in ferromagnetic junctions, *Annu. Rev. Mater. Sci.* 29(1), 381 (1999)
46. S. W. Jiang, S. Liu, P. Wang, Z. Z. Luan, X. D. Tao, H. F. Ding, and D. Wu, Exchange-dominated pure spin current transport in Alq3 molecules, *Phys. Rev. Lett.* 115(8), 086601 (2015)
47. P. A. Bobbert, W. Wagemans, F. W. A. Van Oost, B. Koopmans, and M. Wohlgenannt, Theory for spin diffusion in disordered organic semiconductors, *Phys. Rev. Lett.* 102(15), 156604 (2009)
48. Z. G. Yu, F. Ding, and H. Wang, Hyperfine interaction and its effects on spin dynamics in organic solids, *Phys. Rev. B* 87(20), 205446 (2013)
49. A. Chainani, T. Yokoya, T. Morimoto, T. Takahashi, and S. Todo, Electronic structure of Fe_3O_4 across the Verwey transition, in: Proceedings of the 11th International Conference on Vacuum Ultraviolet Radiation Physics, Elsevier 99, (1996)
50. J. Rackham, B. Pratt, D. Griner, D. Smith, Y. Cai, R. G. Harrison, A. Reid, J. Kortright, M. K. Transtrum, and K. Chesnel, Field-dependent nanospin ordering in monolayers of Fe_3O_4 nanoparticles throughout the superparamagnetic blocking transition, *Phys. Rev. B* 108(10), 104415 (2023)
51. S. Bandyopadhyay, Dominant spin relaxation mechanism in compound organic semiconductors, *Phys. Rev. B* 81(15), 153202 (2010)
52. D. S. McClure, Spin–orbit interaction in aromatic molecules, *J. Chem. Phys.* 20(4), 682 (1952)
53. M. Blume and R. E. Watson, Theory of spin–orbit coupling in atoms. I. Derivation of the spin–orbit coupling constant, *Proc. R. Soc. Lond. A* 270(1340), 127 (1962)
54. G. Bihlmayer, Y. M. Koroteev, P. M. Echenique, E. V. Chulkov, and S. Blügel, The Rashba-effect at metallic surfaces, *Surf. Sci.* 600(18), 3888 (2006)
55. A. Mugarza, C. Krull, R. Robles, S. Stepanow, G. Ceballos, and P. Gambardella, Pietro Gambardella, Spin coupling and relaxation inside molecule–metal contacts, *Nat. Commun.* 2(1), 490 (2011)
56. G. Heimel, I. Salzmann, S. Duhm, and N. Koch, Design of organic semiconductors from molecular electrostatics, *Chem. Mater.* 23(3), 359 (2011)